Article

$P2_1/c$ Postorthopyroxene γ-LiScGe$_2$O$_6$, a New Dense High-Pressure Polymorph and Its Direct Transformation from the $Pbca$ Structure

Martin Ende,* Johannes M. Meusburger, Manuela Zeug, Katharina S. Scheidl, Günther J. Redhammer, and Ronald Miletich

Cite This: *Inorg. Chem.* 2020, 59, 17981−17991

Read Online

ACCESS | Metrics & More | Article Recommendations | Supporting Information

ABSTRACT: Orthorhombic β-LiScGe$_2$O$_6$ single crystals were compressed hydrostatically up to 10.35 GPa using a diamond anvil cell and investigated in situ by means of X-ray diffraction and Raman spectroscopy. Crystal-structure investigations at ambient conditions and at high pressure show a structural transition from an orthopyroxene-type $Pbca$ structure ($a \approx 18.43$ Å, $b \approx 8.85$ Å, and $c \approx 5.34$ Å at 8.6 ± 0.1 GPa) to a postorthopyroxene type $P2_1/c$ structure of the new dense γ-LiScGe$_2$O$_6$ ($a \approx 18.62$ Å, $b \approx 8.85$ Å, $c \approx 5.20$ Å, and $\beta \approx 93.1°$ at 9.5 ± 0.1 GPa). The structure refinements reveal displacive shifts of O atoms associated with a rotation of every other tetrahedral-chain unit from the O- to S-type position similar to the postorthopyroxene-type MgSiO$_3$. As a consequence of the oxygen displacement, the coordination number of Li atoms is changing from $[5 + 1]$ to a proper 6-fold coordination. The transition around $P_c = 9.0 \pm 0.1$ GPa is associated with a volume discontinuity of $\Delta V = -1.6\%$. This orthopyroxene (OEn-$Pbca$) to postorthopyroxene (pOEn-$P2_1/c$) transition is the second example of this type of transformation. Precise lattice parameters have been determined during isothermal compression. The fit of the unit-cell volumes of β-LiScGe$_2$O$_6$, using a third-order Birch−Murnaghan equation of state, yields $V_0 = 943.63 \pm 0.11$ Å^3, $K_0 = 89.8 \pm 0.6$ GPa, and dK/d$P = 4.75 \pm 0.18$ as parameters. Evaluation of the data points beyond the critical transition pressure using a second-order Birch−Murnaghan equation suggests $V_0 = 940.6 \pm 4.4$ Å^3 and $K_0 = 82.4 \pm 4.8$ GPa. A series of high-pressure Raman spectra confirm the symmetry-related structural transition, with band positions shifting in a noncontinuous manner, thus confirming the proposed first-order transition.
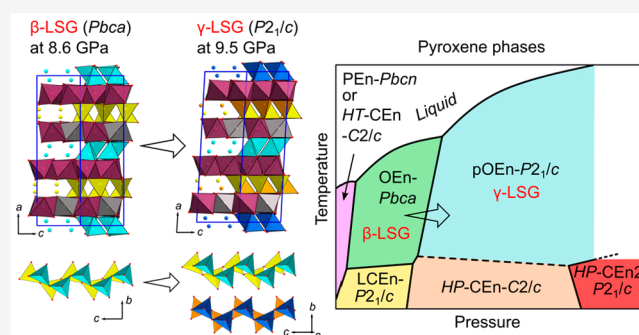
1. INTRODUCTION

Lithium homologues of the pyroxene structure family have recently come into the focus of interest in the search for novel multiferroic materials, especially because monoclinic LiMT$_2$O$_6$ and NaMT$_2$O$_6$ representatives (T = tetrahedral void occupied by, e.g., Si and Ge; M = octahedral void, occupied by, e.g., Sc, In, and Fe) exhibit orbital-assisted spin-Peierls transitions and magnetically driven ferroelectric properties.[1−7] Pyroxenes M1M2T$_2$O$_6$ occur in nature as rock-forming inosilicate minerals[8] and are known for their wide crystallographic versatility, which includes the two major subgroups of orthorhombic *orthopyroxenes* and monoclinic *clinopyroxenes*. Considering the structural modularity and unit-cell twinning-based polytypism for observed crystallographic variations,[9] structural diversifications have been explained based on variations within the infinite tetrahedral−octahedral−tetrahedral "I-beam" units and associated stacking sequences.[10,11] Essential features for distinguishing the structural variants are the TO$_4$-unit rotations in the T-chains (rotation of the S and O type) and the relative orientations of the octahedral M layers (M+ and M−).[10−12]

Because major parts of the Earth's upper mantle consist of silicate pyroxenes, these isostructural compounds have been the subject of systematic studies of thermomechanical behavior and structure−property relationships, in particular with regard to temperature (T) and pressure (P) variations (cf. selected examples[13−19]). A rich polymorphism has been reported that includes the following four archetype phases, referred to as "enstatite" (En) based on the MgSiO$_3$ composition: *high-clinoenstatite* HCEn ($C2/c$), *low-clinoenstatite* LCEn ($P2_1/c$), *orthoenstatite* OEn ($Pbca$), and *protoenstatite* PEn ($Pbcn$).[20] The acentric structure variants, such as $P2_1cn$, are derived from a distorted PEn-$Pbcn$ structure.[21] Other exceptional symmetries, i.e. $P2_1/n$ and $P\overline{1}$, have so far only been found for individual representatives, such as LiAlGe$_2$O$_6$[22] or NaTi-
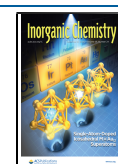
Si_2O_6.[23,24] HCEn ($C2/c$) occurs in two variants, i.e., a unquenchable high-pressure (HP) form (HP-CEn[25,26]) and a quenchable high-temperature phase (HT-CEn[27]). A comparable distinction has to be made for the $P2_1/c$ pyroxenes, where, in addition to the low-clinopyroxene form (LCEn-$P2_1/c$[28]), HP variants (referred to as "HP-CEn2" or "HP-$P2_1/c$" in the literature) have recently been found for several representatives.[29−32]

Because of diverse polytypism, pyroxene structures were the subject of early studies on the course of phase transformation and the associated transformation mechanisms. Most prominent are the transitions between $C2/c$ and $P2_1/c$, which are relevant for discontinuities in the seismic wave propagation within the Earth's upper mantle.[33,34] $LiAlSi_2O_6$ (spodumene) represents one of the archetype structures (HT-CEn-$C2/c$), which was investigated for T and P variations. It shows a distinct displacive first-order phase transition from HT-CEn-$C2/c$ to LCEn-$P2_1/c$.[16,35,36] The equivalent phase transition was reported for $LiScSi_2O_6$ and $ZnSiO_3$.[35] $ZnSiO_3$ was found to be one of the few examples showing a transition sequence upon isothermal compression at 298 K starting from HT-CEn-$C2/c$ to LCEn-$P2_1/c$ and continuing later to HP-CEn-$C2/c$. The second step corresponds to the well-known transformation reported for $Mg_2Si_2O_6$ and $Fe_2Si_2O_6$.[25,26,37] At considerably higher pressures, HP-CEn-$C2/c$ structures undergo a further pressure-induced transition to the so-called "HP-$P2_1/c$" (here further referred to as HP-CEn2-$P2_1/c$), whereby part of the T cations transform to a 6-fold octahedral coordination.[30−32]

Germanate-analogue phases were already in focus early on because the larger Ge atoms were supposed to provide easier access to equivalent HP phases. Regardless of Si or Ge on the T sites, it is the relative size of the individual cations and their interplay at the T, M1, and M2 positions in the $M2M1T_2O_6$ compounds that control the structural stabilities and transformations (e.g., ref 38). The exceptional $P2_1/n$ germanate spodumene homologue, $LiAlGe_2O_6$, was found to transform to LCEn-$P2_1/c$.[39] Hydrostatic compression of the LCEn-$P2_1/c$ spodumene analogue α-$LiScGe_2O_6$ shows no phase transition up to the hydrostatic limit of the pressure-transmitting medium at ∼10 GPa.[40] With regard to the ongoing systematic investigations on lithium pyroxene representatives, we have now conducted a compression study under comparable conditions on the β-$LiScGe_2O_6$ orthopyroxene of the OEn-$Pbca$ type. The aim of this study was to understand the stability criteria from a structural point of view, any polymorphism, and the mechanisms of underlying transitions at nonambient pressure conditions.

2. MATERIALS AND METHODS

Synthesis. Single-crystal synthesis of the orthorhombic form of β-$LiScGe_2O_6$ (β-LSG) was achieved using stoichiometric mixtures of Li_2CO_3, GeO_2, and Sc_2O_3. Crystallization was promoted by following a flux-growth method using a mixture of Li_2MoO_4 (8 parts) and $LiVO_3$ (2 parts) as the high-T solvent. The weight proportion between the stoichiometric nutrient materials and flux components was about 1:10. The mixtures of finely ground solid starting materials were placed in a platinum crucible and slowly heated to the target T of 1323 K at a rate of 3 K min^{-1}; going higher in the target temperature yields the formation of monoclinic α-$LiScGe_2O_6$.[40] After annealing for 24 h, the sample was cooled over 250 h at a rate of −0.03 K min^{-1} to 873 K. After quenching to room temperature, the remnant flux was dissolved in hot distilled water. This synthesis route results in euhedral, idiomorphically shaped, colorless crystals of up to

2 mm in size (Figure S1). Selected crystals were checked by means of energy-dispersive X-ray spectroscopy for element substitutions from flux components. All investigated crystals reveal contents well below the detection limit and confirm the absence of any significant Mo and V substitution.

HP Sample Environment. Selected crystal fragments of suitable size and sufficient optical quality were loaded into ETH-type[41] diamond anvil cells (DACs) using a conventional mixture of 4:1 methanol−ethanol as a pressure-transmitting medium. The pressure chamber, prepared in a stainless-steel gasket, had a starting diameter of 250 ± 5 μm and an initial thickness of around 98 ± 3 μm. The experiments were carried out using DACs with a culet-face diameter of 600 μm. Two to three small ruby spheres (∼12 μm) were used for P determination from their ruby R1 luminescence line.[42]

Lattice Parameter and Isothermal Equation of State (EoS). Precise pressures, as required for the EoS determination, were obtained from the volume data of an extra quartz standard crystal (40 × 40 × 20 μm^3), applying the quartz gauge calibration data.[43] Thus, single-crystal X-ray diffraction (scXRD) used the 8-position centering technique.[44] The sample-crystal size was approximately 100 × 70 × 50 μm^3. The setting angles of approximately 20 Bragg peaks were recorded using a Huber 5042 four-circle diffractometer with Mo K$\alpha_{1,2}$ radiation ($\lambda \approx$ 0.71 Å) from a conventional fine-focus sealed tube source. The software $SINGLE$[45] was used for controlling the diffractometer and to determine the lattice parameters and unit-cell volumes by applying refinements with symmetry-constraint vector least squares. The pressure for the individual data sets taken for this isothermal compression study ranges from ambient conditions up to around 10 GPa. Prior to fitting an EoS equation, f−F plots[46] were used to evaluate the influence of the pressure derivatives K' and K'' on reproduction of the compressibility given by the P−V data points. Finally, the EoS parameters were determined by fitting a third-order Birch−Murnaghan (BM) equation[46] using the analytical software $EoSFit7$.[47,48]

HP Crystal Structure. X-ray intensity data sets were recorded from a single-crystal sample mounted in a DAC with Boehler-Almax-type anvils.[49] Again, the sample-crystal size was about 100 × 70 × 50 μm^3 (Figure S2). The scXRD data were collected using a Stoe StadiVari diffractometer, a molybdenum 50 W air-cooled Incoatec microfocus source, high-brilliance 2D-focusing Quazar multilayer optics, and a Dectris Pilatus 300 K pixel detector with a 450 μm Si layer. Data collection was achieved by ω scans with a 0.5° step width and 50, 70, and 90 s of exposure time per frame (for ambient pressure, 8.6 and 9.5 GPa, respectively). Further experimental details on the instrument settings, subsequent data reduction, and data resolution are summarized in Table 1. At ambient pressure, the reflection conditions were consistent with the orthorhombic space group $Pbca$, while at pressures higher than ∼9 GPa, they were consistent with the monoclinic space group $P2_1/c$. Careful inspection of the reconstructed reciprocal space suggests the existence of twinning of two monoclinic crystal domains for the $P2_1/c$ structure (Figure 1). The measurements as well as the integration, scaling, and numerical absorption correction were performed by applying the X-$AREA$ (Stoe & Cie GmbH) and $Absorb7$[50] software packages. The measurements at ambient pressure were carried out on the sample outside the DAC mounted on a glass fiber. All structure refinements were performed with $SHELXL$[51] and the graphical user interface $ShelXle$[52] based on the structure models reported earlier.[29,53] For twin refinement at 9.5 ± 0.1 GPa, both crystal domains were integrated into an hklf5 file and $Mergehklf5$[54] was used for merging the data sets. The resulting crystal structures were validated with checkCIF/$Platon$[55] for integrity and consistency.

HP Raman Spectroscopy. A LabRam HR800 spectrometer from Horiba Jobin Yvon with backscatter geometry and a Si-based Peltier-cooled CCD detector was used to monitor the P-induced band shifts of the R1 luminescence line of ruby, in order to monitor and adjust the pressure inside the pressure chamber. The calibration terms for the band shift reported by Chijioke et al.[56] were used to derive the pressure values. The same LabRam HR800 instrument was used for acquisition of the in situ Raman spectra of the sample. For both measurements, a grating with 1800 grooves mm^{-1} was used in

Table 1. Crystal Data, Parameters of the scXRD Data Collection, and Results of the Structure Refinements

	pressure (GPa)/temperature (K)		
	10^{-4}/298	8.6(1)/298	9.5(1)/298
space group (No.)	Pbca (61)	Pbca (61)	$P2_1/c$ (14)
a (Å)	18.856(3)	18.428(2)	18.617(13)
b (Å)	9.125(1)	8.853(1)	8.849(1)
c (Å)	5.484(1)	5.342(1)	5.198(1)
β (deg)			93.13(5)
V (Å³)	943.6(3)	871.5(2)	855.1(2)
Z	8	8	8
measd reflns	52368	10947	15928[a]
unique reflns	3471	573	1078[a]
all/obsd reflns	3992	678	1218[a]
max 2θ	91.05	69.19	69.53
exposure time (s)	52	70	90
R_{int}	0.026	0.029	b
R_σ	0.011	0.014	0.015
R1(obs)[c]	0.013	0.029	0.031
R1(all)	0.018	0.037	0.037
wR2	0.024	0.070	0.083
GOF	1.014	1.122	1.060
refined parameter	101	66	90
weighting param (a/b)	0.013/0	0.039/2.64	0.052/2.78
max/min e⁻ density (e Å⁻³)	0.49/−0.51	0.84/−0.56	1.42/−1.27

[a]hklf5, two twin domains. [b]Not calculated, due to hklf5. [c]Intensity-(obs) $\geq 3\sigma$.
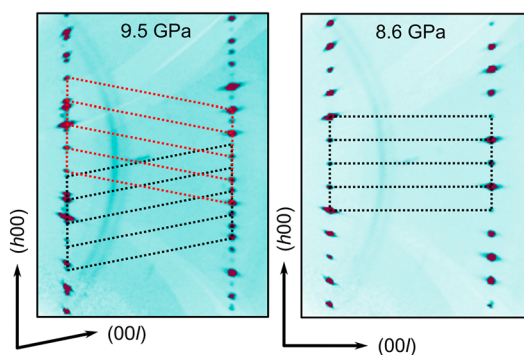
Figure 1. Reconstructed *h0l*-plane sections of the reciprocal space as derived from the measured XRD image series collected at 8.6 ± 0.1 GPa (right) and 9.5 ± 0.1 GPa (left). Unit cells (dotted lines) with base vectors corresponding to the *a** and *c** reciprocal vector lengths are superimposed with the reconstructed sections in this projection down the [010] zone axis. While the reciprocal space at 8.6 GPa can be indexed based on an orthorhombic *Pbca* single-domain lattice, the pattern of reconstructed Bragg peaks at 9.5 GPa suggests the existence of two twinned lattices of monoclinic symmetry related to twin domains rotated by 180° around the former orthorhombic *c* axis.

combination with a 532 nm Nd:YAG laser and an Olympus 50× objective with a 10.6-mm-long working distance. Wavenumber calibration was done using the laser Rayleigh line, and Raman-band fitting was done with *PeakFit4* (Systat Software Inc.) by assuming mixed Lorentzian−Gaussian band shapes after subtraction of the background. The reported uncertainties for the ruby pressure values correspond to the standard deviation, as determined from different rubies within the DAC.

3. RESULTS AND DISCUSSION

Evidence for Transformations in Raman Spectra. A series of HP Raman spectra were measured within the

hydrostatic limit of the used pressure medium up to 9.94 ± 0.15 GPa, in two different orientations of the β-LSG crystals relative to the direction of laser-beam polarization. The two orientations of the randomly mounted idiomorphically shaped sample crystal were rotated by 90° and maintained throughout the whole series between 0.66 and 9.94 GPa. Two series of subsequent 20 spectra each were recorded within the spectral range of 40−1200 cm⁻¹ (Figures 2 and S3 and S4).

A uniform development can be seen in both series of spectra, which is accompanied by a clearly recognizable change in the pressure interval between 8.92 ± 0.09 and 9.09 ± 0.08 GPa. The observed changes in the band positions, relative intensities, and number of bands clearly suggest a phase transformation with the corresponding structural changes. The recorded spectra are rich in vibrational modes especially after the phase transition, which can be attributed to symmetry breaking from orthorhombic to monoclinic lattice metrics if compared to other model pyroxenes.[57−59] For orthorhombic *Pbca* pyroxenes, factor group analysis shows 120 Raman-active modes (30 A_g, 30 B_{1g}, 30 B_{2g}, and 30 B_{3g}); in the new HP monoclinic $P2_1/c$ pyroxene, factor group analysis predicts also 120 Raman-active modes (60 A_g and 60 B_g); in contrast, the $P2_1/c$ pyroxenes at room conditions have only 60 Raman-active modes (30 A_g and 30 B_g).[60,61] The most prominent bands are due to the vibrational modes of the tetrahedral GeO_4 units[62] in the wavenumber range of 500−950 cm⁻¹. They are equivalent to the SiO_4 modes of related pyroxene-type silicates[62,63] but shifted to lower wavenumbers.

Pressure-dependent evolution of the Raman bands reveals clear changes with respect to the number and wavenumber positions of these bands (cf. Figures 2 and 3 as well as Figures S3 and S4). The apparent spectral changes suggest a first-order character of the transition and imply a change in symmetry from the orthorhombic (β-LSG) to probably monoclinic (γ-LSG). The Raman bands above and below the critical transition pressure undergo a smooth evolution with a typical blue shift toward higher energy due to the expected *P*-induced frequency increase of the vibrational modes. The investigated *P*-dependent Raman band positions show an apparently linear and smooth evolution of all bands with a typical dν/dP between +0.98(4) and +4.25(7) cm⁻¹/GPa. Some small Raman bands between 800 and 1000 cm⁻¹ possibly originate from the 4:1 methanol−ethanol mixture used as a pressure-transmitting medium and show a different linear behavior in the *P*-induced band-shift evolution. Furthermore, a new band seems to arise at 6 GPa around 870 cm⁻¹, which could be associated with a continuous coordination change of the Li cation mentioned in the crystal structure part below. It would be conceivable that the Li atom dynamically switches between two positions under standard conditions and, after a certain pressure, remains in a position where it has a higher coordination, for instance, [6] instead of [5 + 1]. This would change the number and intensity of the Raman bands, as observed, e.g., for dynamic disordered H_2O molecules and OH groups.[64]

Isothermal Compressibilities and EoS. Symmetry-unconstrained vector least-squares fits to the corrected diffractometer setting angles were applied in a first step to prove the lattice metrics at individual pressure points. According to the findings, constrained refinements were applied to derive the values for the lattice parameters (Figure 4) listed in Table S1. Below 9 GPa, the refined values of α, β, and γ for β-LSG correspond to 90° within an uncertainty of
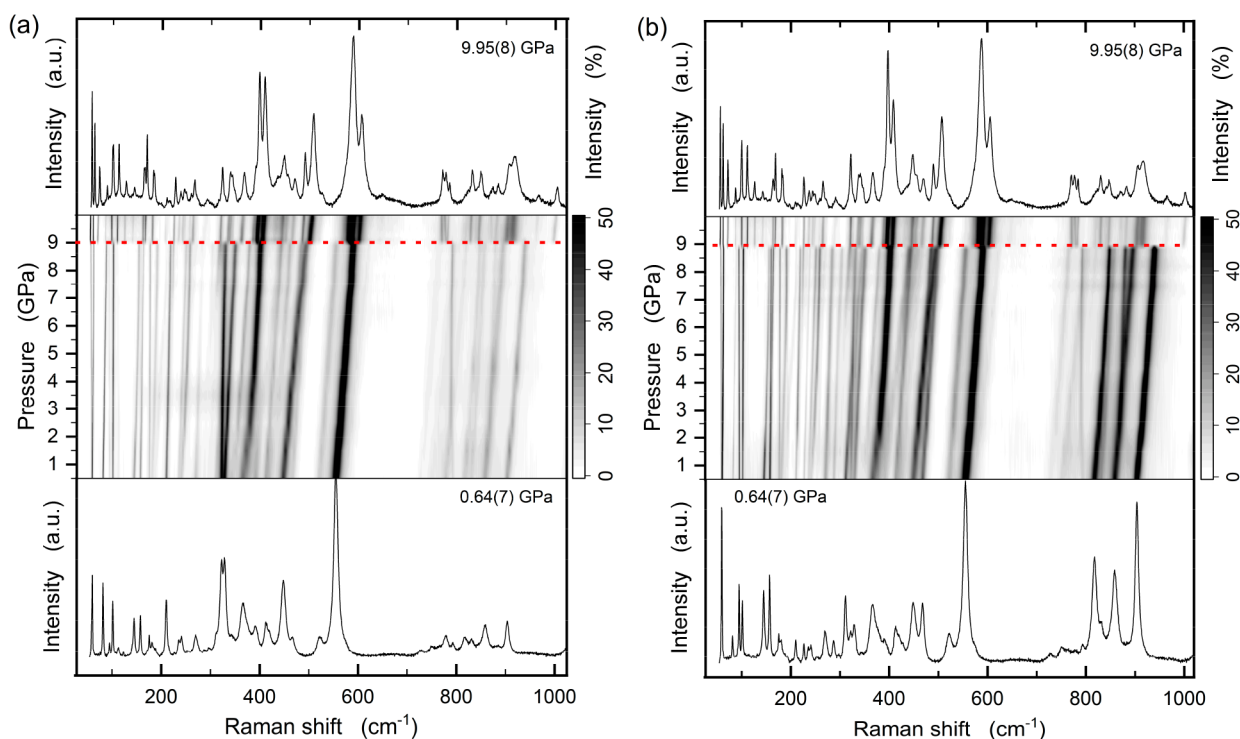
Figure 2. Variation of the Raman spectra of LSG at hydrostatic HP conditions in a sequence of isothermal compression (T = 298 K) from 0.64(7) to 9.95(8) GPa in two orientations (a and b) with the laser polarization vector rotated by 90°. In both series, a distinct change at ~9 GPa indicates the occurrence of a phase transition. Some small Raman bands between 800 and 1000 cm^{-1} possibly originate from the 4:1 methanol−ethanol mixture showing a different linear behavior in the P-induced band-shift evolution.
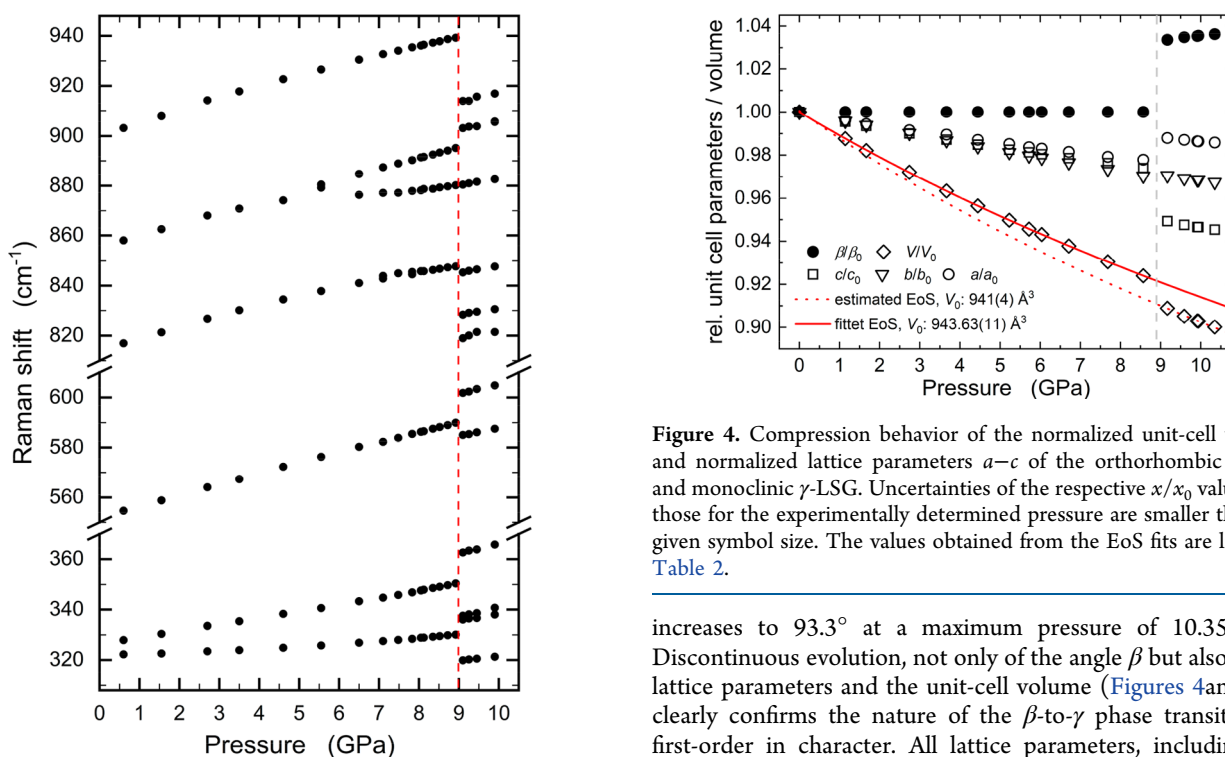

Figure 3. Positional Raman shifts of selected representative bands of LSG as a function of the pressure upon isothermal compression. Shown are only intense, selected bands.

Figure 4. Compression behavior of the normalized unit-cell volume and normalized lattice parameters $a-c$ of the orthorhombic β-LSG and monoclinic γ-LSG. Uncertainties of the respective x/x_0 values and those for the experimentally determined pressure are smaller than the given symbol size. The values obtained from the EoS fits are listed in Table 2.

increases to 93.3° at a maximum pressure of 10.35 GPa. Discontinuous evolution, not only of the angle β but also for all lattice parameters and the unit-cell volume (Figures 4 and S5), clearly confirms the nature of the β-to-γ phase transition as first-order in character. All lattice parameters, including the unit-cell volume, show clear discontinuities in the pressure evolution. The volume data reveal a spontaneous decrease in ΔV by about −1.6% and are comparable to many first-order transitions in pyroxene-type structures.[16,23,25,26,35−37,39] The discontinuity can also be seen in the crystallographic axes, with a strong shortening of the lattice periodicity along the c axis (−2.6%), while in the a- and b-axis directions, changes across

less than ±0.01°. Beyond 9 GPa, the angle β spontaneously increases within a short interval to 93.0°, which further

Table 2. Least-Squares-Fitted BM3-EoS Parameters of the Unit-Cell Volumes and Lattice Parameters for β-LSG and γ-LSG

	orthorhombic LSG at 0–9 GPa			monoclinic LSG above 9 GPa		
	X_0/V_0 [Å^3]	M_0/K_0 [GPa]	M'/K'	X_0/V_0 [Å^3]	M_0/K_0 [GPa]	M'/K'
V	943.63(11)	89.8(6)	4.75(18)	940.6(4.4)	82.4(4.8)	4 fixed[a]
a	18.856(3)	296(8)	20.7(2.3)	19.008(12)	403(13)	12 fixed[a]
b	9.1248(6)	266(3)	5.1(6)	9.113(27)	268(31)	12 fixed[a]
c	5.4843(4)	248(4)	21.1(1.1)	5.430(14)	168(13)	12 fixed[a]

[a]Because of a limited number of data points, a BM2-EoS is used here.

Table 3. Atomic Coordinates and Displacement Parameters of β-LSG at 10^{-4} GPa (Ambient Pressure, aP) and 8.6 GPa as well as γ-LSG at 9.5 GPa

				aP					
	x	y	z	U_{eq}		x	y	z	U_{eq}
GeA	0.47291(2)	0.66284(2)	0.28415(2)	0.00492(1)	O2	0.18260(2)	0.67104(5)	0.54917(7)	0.00622(5)
GeB	0.27526(2)	0.66067(2)	0.55489(2)	0.00501(1)	O3	0.43346(2)	0.50354(5)	0.18946(8)	0.00881(6)
Li	0.62453(9)	0.49241(19)	0.1268(3)	0.0211(3)	O4	0.44568(2)	0.80612(5)	0.08880(8)	0.00862(6)
Sc	0.37572(2)	0.35124(2)	0.37429(2)	0.00494(1)	O5	0.31030(2)	0.77947(5)	0.33580(8)	0.00990(6)
O1	0.56621(2)	0.66787(5)	0.29511(7)	0.00646(5)	O6	0.30869(2)	0.48649(5)	0.54397(9)	0.01051(6)
				8.6 GPa					
	x	y	z	U_{eq}/U_{iso}		x	y	z	U_{eq}/U_{iso}
GeA	0.47034(3)	0.66444(6)	0.28992(7)	0.0063(2)[a]	O2	0.1816(2)	0.6678(4)	0.5316(5)	0.0074(6)
GeB	0.27513(3)	0.65846(6)	0.54569(7)	0.0065(2)[a]	O3	0.4321(2)	0.5068(4)	0.1672(5)	0.0092(7)
Li	0.6222(6)	0.4853(12)	0.1480(14)	0.0153(18)	O4	0.4445(2)	0.8211(4)	0.1079(5)	0.0087(6)
Sc	0.37673(5)	0.35002(11)	0.36109(13)	0.0056(2)[a]	O5	0.3131(2)	0.7793(4)	0.3280(5)	0.0098(7)
O1	0.5646(2)	0.6661(4)	0.3038(5)	0.0072(6)	O6	0.3057(2)	0.4771(4)	0.5393(5)	0.0121(7)
				9.5 GPa					
	x	y	z	U_{eq}/U_{iso}		x	y	z	U_{eq}/U_{iso}
GeA1	0.47010(4)	0.66326(9)	0.29495(11)	0.0059(2)[a]	O2A	0.1832(3)	0.6665(5)	0.5438(7)	0.0074(7)
GeA2	0.02686(4)	0.33952(8)	0.79780(10)	0.0059(2)[a]	O2B	0.3174(3)	0.3334(6)	−0.0253(7)	0.0074(7)
GeB1	0.27566(5)	0.65945(8)	0.53983(11)	0.0063(2)[a]	O3A	0.4356(3)	0.5059(6)	0.1504(7)	0.0076(6)
GeB2	0.22466(5)	0.34114(8)	−0.04743(10)	0.0063(2)[a]	O3B	0.0643(3)	0.4972(6)	0.6754(7)	0.0076(6)
LiA	0.6176(8)	0.4854(17)	0.1779(19)	0.014(3)	O4A	0.4414(3)	0.8225(5)	0.1121(7)	0.0070(6)
LiB	0.8749(8)	0.5207(17)	0.6285(19)	0.016(3)	O4B	0.0558(3)	0.1804(6)	0.6255(7)	0.0070(6)
ScA	0.37605(7)	0.35114(15)	0.32029(18)	0.0050(2)[a]	O5A	0.3093(3)	0.8055(6)	0.3573(7)	0.0072(6)
ScB	0.12475(7)	0.64765(16)	0.87282(18)	0.0050(2)[a]	O5B	0.1923(3)	0.3103(6)	0.6330(7)	0.0072(6)
O1A	0.5633(3)	0.6684(5)	0.3315(7)	0.0068(6)	O6A	0.3123(3)	0.4877(6)	0.4883(7)	0.0099(7)
O1B	0.9337(3)	0.3331(5)	0.8003(7)	0.0068(6)	O6B	0.1893(3)	0.5028(6)	0.0694(7)	0.0099(7)

[a]U_{eq}.

the transition point yield opposite signs ($+1.0\%\|a$ and $+0.02\%\|b$). This behavior can be explained by changes to the tetrahedron chains and is proven for several other pyroxene transformations.[16,23,25,26,35–37,39]

The pressure–volume (P–V) data were analyzed with respect to the volume compression properties. The corresponding isothermal EoS is usually parametrized in terms of the values of the bulk modulus (K) and its pressure derivatives $K' = dK/dP$ and $K'' = dK'/dP$. In a plot of normalized $P(F)$ versus Eulerian strain (f_E) (Figure S6), the trend line follows a relationship in a linear fashion with a clearly positive slope, which indicates that K' must be significantly larger than 4. Accordingly, a third-order BM EoS appears to be appropriate for the P–V data below 9 GPa for β-LSG. Weighted fits return reasonably small uncertainties for the calculated parameters V_0, K_0, and K', as well as for x_0, M_0, and M' describing the compressibilities of the individual crystallographic axes (Table 2). Any attempt to fit higher order, i.e., a fourth-order BM-EoS, only brings marginal deviations for K'' with respect to its implied uncertainty [$K'' = -0.05(29)$]. The bulk modulus of 89.8 ± 0.6 GPa, as obtained by the third-order BM-EoS,

compares to equivalent orthopyroxene structures and follows the systematics of the Anderson–Anderson relationship.[65] The axial moduli (Table 2) are very similar ($M_0 = 296 \pm 8$ GPa$\|a$, 266 ± 3 GPa$\|b$, and 248 ± 4 GPa$\|c$), even compared to those of monoclinic α-LSG ($M_0 = 225$ GPa$\|a$, 277 GPa$\|b$, and 226 GPa$\|c$[40]), showing a nearly isotropic compression of β-LSG. The volume compression V/V_0 at 10 GPa is nearly the same as that observed for α-LSG. Compared to other ortho- and clinopyroxenes in a plot versus the unit-cell volume at ambient conditions (Figure S7), it possesses a relatively large volume compression, together with a large unit cell, and therewith it probably continues the trend observed by Hofer et al. (2015)[40] for clinopyroxenes, although the data for orthopyroxenes are still a bit sparse.

Attempts to fit the equivalent moduli for γ-LSG are much more difficult because of the short pressure interval between 9.0 and 10.35 GPa. Equivalent fits finally based on BM2-EoS (K' and M' fixed to 4 and 12; Table 2) yield $K_0 = 82.4 \pm 4.8$ GPa, $M_0 = 403 \pm 13$ GPa$\|a$, 268 ± 31 GPa$\|b$, and 168 ± 13 GPa$\|c$. The bulk modulus indicates higher compressibility above the critical transition pressure, although the monoclinic

Table 4. Interatomic Distances of β-LSG at 10^{-4} and 8.6 GPa and γ-LSG at 9.5 GPa

	10^{-4} GPa	8.6(1) GPa	9.5(1) GPa		10^{-4} GPa	8.6(1) GPa	9.5(1) GPa
Li−O1	2.151(2)	2.093(11)	2.090(15)/2.155(15)[a]	Sc−O1	2.1252(5)	2.096(3)	2.088(4)/2.074(5)[b]
Li−O2	2.188(2)	2.175(11)	2.184(15)/2.147(15)[a]	Sc−O1	2.2049(5)	2.144(4)	2.147(5)/2.140(5)[b]
Li−O3	2.051(2)	1.960(9)	1.927(12)/1.999(13)[a]	Sc−O2	2.1047(5)	2.068(3)	2.057(4)/2.083(5)[b]
Li−O4	2.660(2)	2.307(10)	2.146(15)/2.262(14)[a]	Sc−O2	2.1984(5)	2.142(4)	2.145(5)/2.139(5)[b]
Li−O5	2.308(2)	2.183(11)	2.109(16)/2.337(14)[a]	Sc−O3	2.0357(5)	2.010(4)	1.998(5)/ 1.992(5)[b]
Li−O6	2.210(2)	2.160(10)	2.127(12)/2.035(13)[a]	Sc−O6	1.9966(5)	1.971(4)	1.935(5)/ 1.999(5)[b]

[a]LiA−OXA/LiB−OXB. [b]ScA−OXA/ScB−OXB.

structure of γ-LSG is denser than that of the LP β-LSG. This can be attributed to elastic softening, as is typical for lithium pyroxenes.[16] Moreover, it is remarkable that γ-LSG shows a more pronounced anisotropic compression behavior compared to both the orthorhombic β-LSG and monoclinic low-pressure α-LSG.

HP Crystal Structures. Structure refinements were carried out at 8.6 and 9.5 GPa, just below and above the critical transition pressure around 9.0 GPa, in addition to one refinement at ambient conditions (cf. Table 1). The observed systematic absences of the XRD intensities confirm space group $Pbca$ for β-LSG at 1 bar and at 8.6 GPa, while they suggest $P2_1/c$ at 9.5 GPa for monoclinic γ-LSG. Because of the restricted number of Fourier coefficients in the given crystal orientation, the HP refinements were carried out with anisotropic displacement parameters only for Sc and Ge atoms, while Li and O atoms were refined using an overall isotropic displacement parameter (cf. Table 3). In contrast, a model with anisotropic displacement parameters for all atoms was used for the refinements at 1 bar, with the crystal mounted on a glass fiber. For refinement of the $P2_1/c$ structure of γ-LSG, a twin domain was additionally indexed, integrated, and refined according to the presence of a 2-fold rotation about the c axis, giving the twin law $[-1\ 0\ (2a\cos\beta)/c\ 0\ -1\ 0\ 0\ 0\ 1]^{[66]}$ with $(2a\cos\beta)/c \approx -0.39$ for γ-LSG at 9.5 GPa. The relationships between the number of refined parameters, observed unique reflections, and resulting reliability indices are listed in Table 1. The obtained positional parameters and isotropic or equivalent displacement parameters are provided in Table 3. The anisotropic displacement parameters for the measurement at 1 bar are listed in Table S2. Selected interatomic distances, relevant bond angles, and octahedral distortion are summarized in Tables 4 and 5.

At first glance, the stereochemistry and bonding relationships between the individual structure variants are not fundamentally different (Figure 5). The coordination geometries of the various building units are almost unchanged, with Ge atoms in tetrahedral coordination and Sc and Li atoms in more or less distorted octahedral arrangements. The bond distances for all Ge atoms (GeA and GeB sites in β-LSG; GeA1, GeA2, GeB1, and GeB2 sites in γ-LSG) and the Sc atoms on the M1 site are in agreement with the expected bond compression variations in the corresponding GeO_4 and ScO_6 units (Tables 4 and S3). The Li atoms, hosted at the M2 site (one Li position in β-LSG; two LiA and LiB positions in γ-LSG), reveal a significant shortening of the individual nonbonding M2−O distances, which only contribute at high P with appropriate bond strengths. The effective coordination number changes gradually from $[4 + 1 + 1]$ to $[5 + 1]$ in β-LSG up to 8.6 GPa and reveals a significant change to a proper 6-fold coordination for both Li sites in γ-LSG (Table 4). Simultaneously, the LiO_6 coordination polyhedra show

Table 5. Characteristic Interatomic Distances (Å) and Angles (°) for the $[Ge_2O_6]_n$ Chains of Orthorhombic and Monoclinic LSG[a]

	10^{-4} GPa	8.6(1) GPa	9.5(1) GPa
GeA−GeA[b]	3.1699(5)	3.0707(7)	3.018(1)/3.044(1)
GeB−GeB[b]	3.1902(5)	3.1243(7)	3.053(1)/3.059(1)
GeA−O4−GeA[c]	127.32(3)	121.0(2)	117.5(3)/118.9(3)
GeB−O5−GeB[c]	130.63(3)	127.8(2)	121.4(3)/120.8(3)
O3−O4−O3[d]	138.69(2)	128.6(2)	128.5(2)/126.4(2)
O6−O5−O6[d]	166.22(2)	166.1(2)	147.1(2)/133.6(2)
O4−O4−O4[d]	139.04(2)	129.53(12)	127.5(2)/129.3(2)
O5−O5−O5[d]	157.81(2)	158.02(14)	138.6(2)/135.4(2)

[a]The distances and angles are calculated according to the crystallographic data given in Table 3. [b]GeA1−GeA1, GeA2−GeA2 respectively GeB1−GeB1, GeB2−GeB2. [c]GeA1−O4A−GeA1, GeA2−O4B−GeA2 respectively GeB1−O5A−GeB1, GeB2−O5B−GeB2. [d]OXA−OXA−OXA, OXB−OXB−OXB.

decreasing polyhedral distortion with increasing P, mainly manifested by the shrinking Li−O4 distance from 2.660(2) Å at ambient conditions to 2.307(10) Å at 8.6 GPa and 2.146(15) Å at 9.5 GPa (cf. Table 4).

The most striking structural change concerns the relative position and orientation of the GeO_4 tetrahedra within the symmetrically individual $[Ge_2O_6]_n$ chains (one type of chain in β-LSG, in contrast to two types in γ-LSG, i.e., the so-called A-chain and B-chain; cf. Figure 5). The symmetry decoupling associated with the transition from the P-centered orthorhombic lattice to a monoclinic P Bravais lattice is also evidenced by a change of the vibrational modes assigned to the GeO_4 tetrahedra themselves as well as modes originating from the vibration dynamics within the parent chain units. In both chain types, which are aligned parallel to the crystallographic c axis, the bridging O atoms (O4 and O5) are subjected to the largest positional shifts. It is not surprising that precisely these atoms show the aforementioned strong changes in the Li−O bond distances, being involved in the reported stereochemical changes around the Li atoms. In detail, the A-site T-chain in β-LSG splits into two T-chains with the O6−O5−O6 angle changing from $166.22 \pm 0.02°$ (at ambient pressure) and $166.1 \pm 0.2°$ (at 8.6 GPa) to $147.1 \pm 0.2°$ and $133.6 \pm 0.2°$ (at 9.5 GPa). The B-site T-chain in β-LSG undergoes a change in the O3−O4−O3 angle from $138.69 \pm 0.02°$ (at ambient pressure) and $128.6 \pm 0.2°$ (at 8.6 GPa) to $128.5 \pm 0.2°$ and $126.4 \pm 0.2°$, which is comparable to that reported for the $P2_1/c$ postorthopyroxene $MgSiO_3$ phase[29] (Figure S8). The large change of angle in the A-chain can be assigned to the splitting of the Raman doublet, whereas the change for the B-chain is so small that the associated peak splitting cannot be resolved, thus yielding only a triplet instead of the expected quadruplet. The atomic displacements involved are more pronounced in the A-
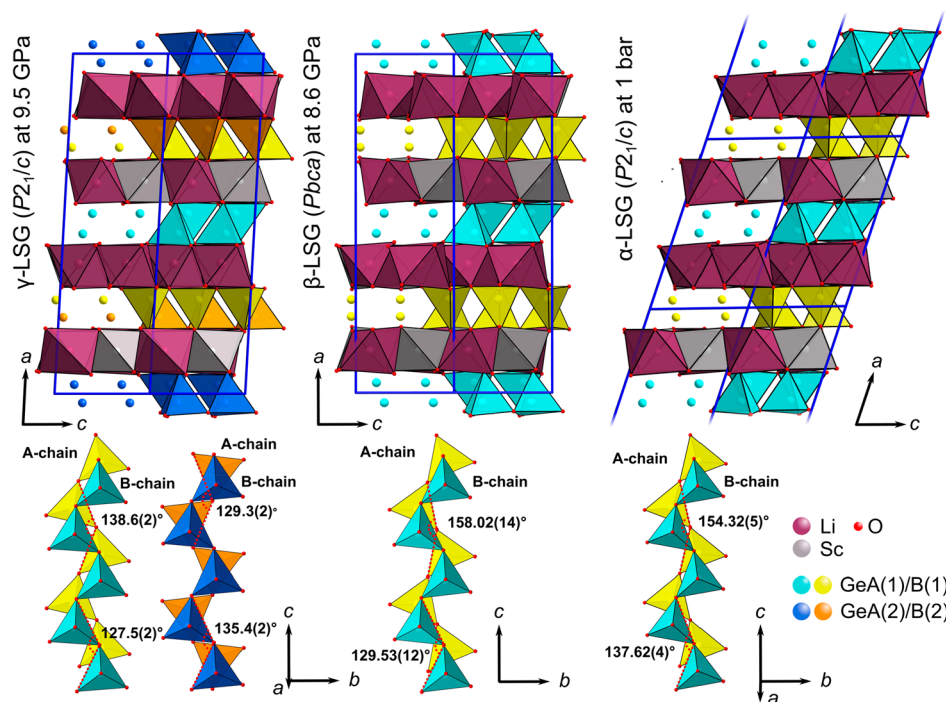
Figure 5. Crystal structures of α-LSG at 9.5 GPa as well as β- and γ-LSG at HP conditions below (8.6 GPa) and above (9.5 GPa) the transition pressure at 9.0 GPa. The structures are shown at the top in a projection of two unit cells along the b axis, and below the GeO$_4$ tetrahedron, chain units can be seen in a view on the bc plane. The most significant changes concerning the O4−O4−O4 and O5−O5−O5 angles, which determine the S-rotated (yellow, GeA) and O-rotated (turquoise, GeB) chains (cf. Figure 6), are marked accordingly.

chain along the a axis toward the center of the unit cell, while the largest displacement in the B-chain occurs within the (100) plane. According to the common nomenclature,[10] the A-chain is S-rotated and the B-chain is O-rotated. Both chain types reveal internal folding, as expressed by all Ge−O4/5−Ge, O4−O4−O4, and O5−O5−O5 angles getting smaller with increasing pressure (Table 5). This corresponds to the compression mechanisms observed in several $P2_1/c$ pyroxenes.[15]

Transformation Pathway of the β-to-γ Transition. Similar to the previous findings,[29] the structure of γ-LSG could not be assigned to any of the established archetypes, to neither orthopyroxene (OEn-$Pbca$), LP-clinopyroxene (LCEn-$P2_1/c$), high-temperature-clinopyroxene (HT-CEn-$C2/c$), nor HP clinopyroxene (HP-CEn-$C2/c$). Despite the same space group ($P2_1/c$), the structure determined for γ-LSG showed clear differences in the β angle or the periodicity length of a, which is evident in the direct comparison between LCEn-$P2_1/c$ α-LSG[40] and γ-LSG (α-LSG, β = 102.9°, a = 9.69 Å; γ-LSG, β = 93.1°, a = 18.86 Å). Both the lattice-metric characteristic and the finding of the γ-LSG structure to be isostructural with the postorthopyroxene type MgSiO$_3$ confirm the existence of a comparable transformation between the orthorhombic OEn-$Pbca$-type β-LSG and the monoclinic postorthopyroxene pOEn-$P2_1/c$-type γ-LSG.

The transformation from OEn-$Pbca$ orthopyroxene to the pOEn-$P2_1/c$ postorthopyroxene structure has so far only been reported for MgSiO$_3$ (Zhang et al., 2012[29]), with half of the tetrahedra in every second layer to change from the original O configuration to S-rotated chain units across the OEn−pOEn transition (Figure S5). As previously reported, the M+ M+ M− M− sequence of the octahedral layer alignment along the a-axis direction, typical for orthopyroxene topology,[10,11] is also

retained here. This makes the pOEn-$P2_1/c$ phase very different from a further HP clinopyroxene phase, which also crystallizes in $P2_1/c$ but has the M+ M+ sequence typical for clinopyroxene phases and is confirmed by the HP-CEn2-$P2_1/c$ structures of various silicate clinopyroxenes.[30−32]

The transition mechanism corresponds to previous predictions[67] and can be interpreted as an incomplete rotation from O- to S-chains within every second tetrahedral layer. According to the established nomenclature,[11] the local stacking sequence within one-fourth of the I-beams has to change from A$^{T(O-rot)}$B^{M}C$^{T(O)}$A to A$^{T(O)}$B^{M}C$^{T(S-rot)}$B. The corresponding O-monolayer stacking sequence thus changes from AB<u>AC</u>BABC (pyroxene no. 10 = OEn-$Pbca$) to ABAB<u>C</u>ABC (pyroxene no. 8b = pOEn-$P2_1/c$). This can be achieved by a simple rotation of the basis triangle of the GeO$_4$ tetrahedra by about 30° (cf. Figure 6). The pure rotation would not be associated with a volume reduction, but only the simultaneous shortening of the Li−O distances (Table 4) by displacing the O atoms within the basic triangle of the GeO$_4$ tetrahedra enables the described reduction in the a-axis direction and in the volume, respectively.

4. CONCLUSIONS

The transformation into the crystallographically new post-orthopyroxene structure type proves the existence of three different polymorphs of LiScGe$_2$O$_6$, i.e., α-LSG (=LCEn-$P2_1/c$ clinopyroxene type), β-LSG (=OEn-$Pbca$ orthopyroxene type), and γ-LSG (=pOEn-$P2_1/c$ postorthopyroxene type). The molar volume, or the relative volume units per formula unit Z, at 1 bar indicate that α-LSG (V/Z = 117.35 Å^3) is the low-T form and β-LSG [$V/(2*Z)$ = 117.95 Å^3] the corresponding high-T form. A comparison of all three phases at 9 GPa, the β-to-γ transformation point, shows from the V/Z volume
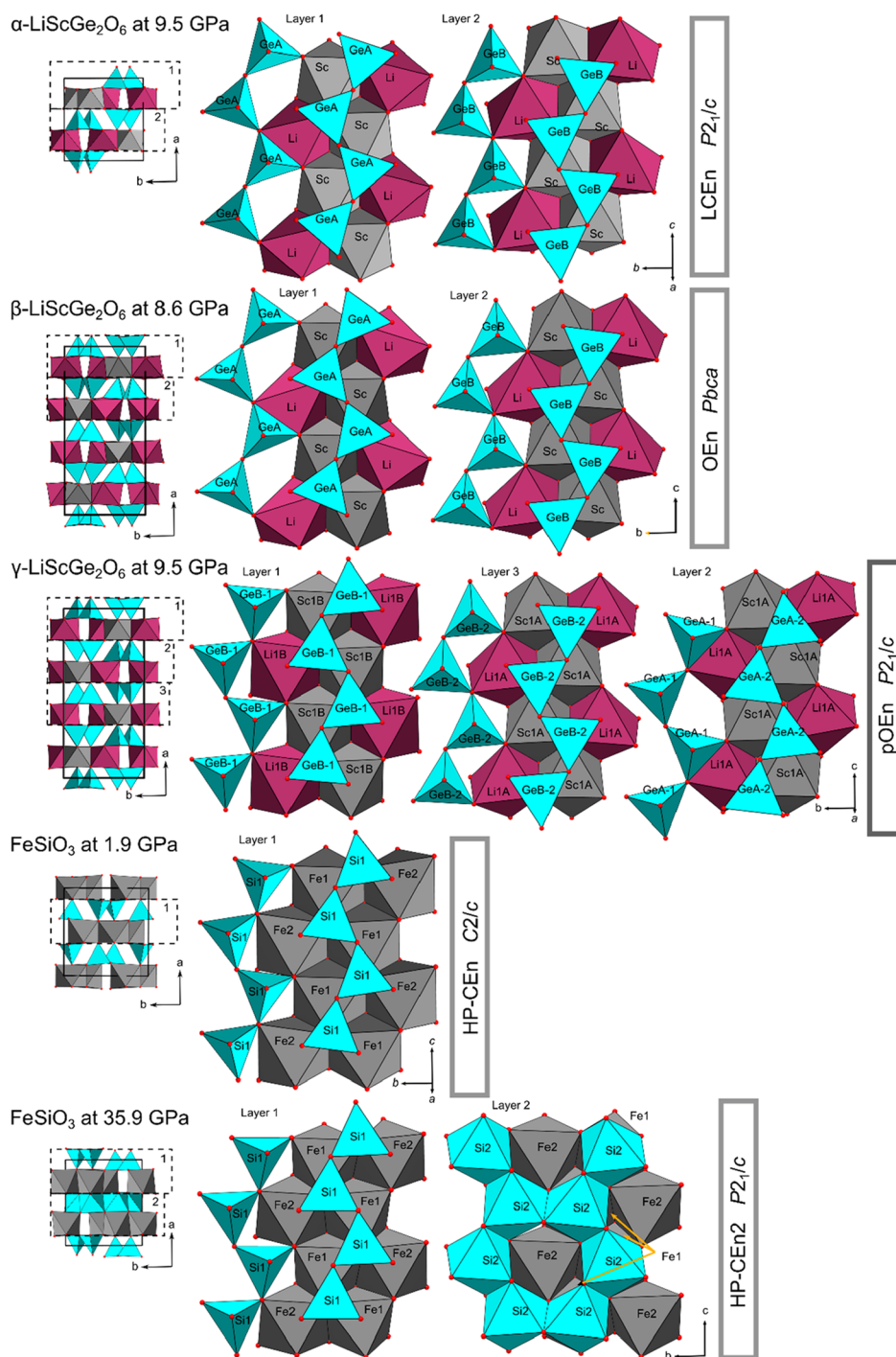
Figure 6. Individual octahedra−tetrahedra bilayer sheets in a polyhedral illustration according to the bilayer sequence along a [following the bilayer labels in the (001) projection on the left side]. The following structures are compared: (a) LCEn-$P2_1/c$, α-LSG[40] at 9.5 GPa; (b) OEn-$Pbca$, β-LSG at 8.6 GPa (this study); (c) pOEn-$P2_1/c$, γ-LSG at 9.5 GPa (this study; see a comparison with $MgSiO_3$ at 14.3 GPa[29] in Figure S8); (d) HP-CEn-$C2/c$, $FeSiO_3$ at 1.9 GPa;[37] (e) HP-CEn2-$P2_1/c$, $FeSiO_3$ at 35.9 GPa.[31]

fractions calculated from the EoS data (α-LSG, 108.13 Å^3; β-LSG, 108.68 Å^3; γ-LSG, 107.33 Å^3) that the new γ phase is the densest and can therefore be assigned as the HP phase in this system. Its density is even higher than that of the β phase at the same pressure conditions. The compressibility of the three phases is extremely similar because the structure topologies of the three phases are also very similar in comparison.

The β-to-γ transition for LSG reported here was predicted[67] and later reported only for $MgSiO_3$ in the pressure interval between 10 and 14.2 GPa.[29] The new dense γ-LSG structure is therefore the second example of this type of phase transition, which in both cases takes place through direct transformation from the OEn-$Pbca$ orthopyroxene structure. Nevertheless, the terms used for the monoclinic HP phases are sometimes confusing because there are at least three different pyroxene

structures with the same space group $P2_1/c$, including the new postorthopyroxene described here, the early-established "low-clinopyroxene" (=LCEn-$P2_1/c$), and the recently described HP-CEn2 structures.[30−32] The latter structure is the one that transforms exclusively from the $C2/c$-type HP forms of the clinopyroxenes (HP-CEn-$C2/c$), whereby every second tetrahedron layer is transformed into an octahedron in the course of a translation between the O monolayers. The former T-cations are thus coordinated octahedra in the sense of the formula $AMT^{[4]}T^{[6]}O_6$. In addition, this $C2/c$-to-$P2_1/c$ transformation retains the typical M+ M+ sequence of the octahedral layer alignment along the a-axis direction, such that the completely different M+ M+ M− M− sequence is preserved for the structurally different $Pbca$-to-$P2_1/c$ orthopyroxene−postorthopyroxene transition, which is reported here.

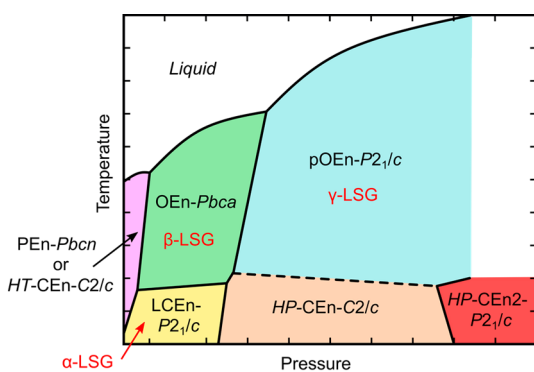A schematic diagram in the sense of a P−T phase diagram (Figure 7) shows the single-phase regions of the relevant

Figure 7. Schematic diagram showing the regions of occurring pyroxene phases in the P−T space. Abbreviations: PEn = protoenstatite (pink field); LCEn = low clinoenstatite (yellow field); HT-CEn = high-temperature clinoenstatite (pink field); HP-CEn = high-pressure clinoenstatite (orange field); HP-CEn2 = high-pressure clinoenstatite-II (red field); OEn = orthoenstatite (green field); pOEn = postorthoenstatite (turquoise field). The three polymorphs of LSG correspond to LCEn-$P2_1/c$ (=α-LSG), OEn-$Pbca$ (=β-LSG), and pOEn- $P2_1/c$ (=γ-LSG).

structures in which the separating lines do not correspond to the proper thermodynamic equilibrium boundaries but rather represent tie lines along which the structural transitions can be expected. The diagram again shows the three different $P2_1/c$ phases (yellow, turquoise, and red) and which phases correspond to the three LSG polymorphs (yellow, green, and turquoise). The diagram also clarifies the confusion regarding the recently published HP forms of $P2_1/c$ symmetry. Referring to the purely displacive character involving rotation of the TO_4 units, it is understandable that the OEn−pOEn transformation takes place at much lower pressures, and the second transition of the HP-CEn structures from $C2/c$ to $P2_1/c$ can only take place at significantly higher pressures because of the change in coordination. It is noteworthy that the HP-CEn-$C2/c$ phase has not been observed yet as another phase during the compression of LSG, which should only be due to the fact that the pressure in previous studies was not high enough. Such a transformation into $C2/c$ and further into the HP-CEn2-$P2_1/c$ structure is therefore very likely.

ASSOCIATED CONTENT

Supporting Information

The Supporting Information is available free of charge at https://pubs.acs.org/doi/10.1021/acs.inorgchem.0c02284.

> Refined pressure-dependent monoclinic and orthorhombic lattice parameters and corresponding plots, observed bond lengths of the GeA and GeB tetrahedra, pressure-dependent Raman waterfall plots, and crystal pictures (PDF)

Accession Codes

CCDC 2020095−2020097 contain the supplementary crystallographic data for this paper. These data can be obtained free of charge via www.ccdc.cam.ac.uk/data_request/cif, or by emailing data_request@ccdc.cam.ac.uk, or by contacting The Cambridge Crystallographic Data Centre, 12 Union Road, Cambridge CB2 1EZ, UK; fax: +44 1223 336033.

AUTHOR INFORMATION

Corresponding Author

Martin Ende − *Institut für Mineralogie und Kristallographie, Universität Wien, A-1090 Wien, Austria;* orcid.org/0000-0002-9509-8543; Email: martin.ende@univie.ac.at

Authors

Johannes M. Meusburger − *Institut für Mineralogie und Kristallographie, Universität Wien, A-1090 Wien, Austria; Camborne School of Mines, University of Exeter, Penryn TR10 9FE, Cornwall, U.K.*

Manuela Zeug − *Institut für Mineralogie und Kristallographie, Universität Wien, A-1090 Wien, Austria*

Katharina S. Scheidl − *Institut für Mineralogie und Kristallographie, Universität Wien, A-1090 Wien, Austria; Department of Physics, Norwegian University of Science and Technology, N-7491 Trondheim, Norway*

Günther J. Redhammer − *Fachbereich Chemie und Physik der Materialien, Universität Salzburg, A-5020 Salzburg, Austria;* orcid.org/0000-0003-0996-3930

Ronald Miletich − *Institut für Mineralogie und Kristallographie, Universität Wien, A-1090 Wien, Austria*

Complete contact information is available at:
https://pubs.acs.org/10.1021/acs.inorgchem.0c02284

Notes

The authors declare no competing financial interest.

REFERENCES

(1) Konstantinević, M. J.; Van Den Brink, J.; Popović, Z. V.; Moshchalkov, V. V.; Isobe, M.; Ueda, Y. Orbital Dimerization in $NaTiSi_2O_6$. An Orbital Analogue of the Spin-Peierls Phase Transition. In *Journal of Magnetism and Magnetic Materials*; North-Holland, 2004; Vol. 272−276, pp E657−E658; DOI: 10.1016/j.jmmm.2003.11.328.

(2) Shirakawa, T.; Ohta, Y.; Mizokawa, T. Orbital Ordering and Spin-Singlet Formation in a Pyroxene Compound $NaTiSi_2O_6$. *Phys. B* **2006**, *378−380*, 1056−1057.

(3) Jodlauk, S.; Becker, P.; Mydosh, J. A.; Khomskii, D. I.; Lorenz, T.; Streltsov, S. V.; Hezel, D. C.; Bohaty, L. Pyroxenes: A New Class of Multiferroics. *J. Phys.: Condens. Matter* **2007**, *19* (43), 432201.

(4) Redhammer, G. J.; Roth, G.; Treutmann, W.; Hoelzel, M.; Paulus, W.; André, G.; Pietzonka, C.; Amthauer, G. The Magnetic

Structure of Clinopyroxene-Type $LiFeGe_2O_6$ and Revised Data on Multiferroic $LiFeSi_2O_6$. *J. Solid State Chem.* **2009**, *182* (9), 2374−2384.

(5) Redhammer, G. J.; Senyshyn, A.; Meven, M.; Roth, G.; Prinz, S.; Pachler, A.; Tippelt, G.; Pietzonka, C.; Treutmann, W.; Hoelzel, M.; Pedersen, B.; Amthauer, G. Nuclear and Incommensurate Magnetic Structure of $NaFeGe_2O_6$ between 5 and 298 K and New Data on Multiferroic $NaFeSi_2O_6$. *Phys. Chem. Miner.* **2011**, *38* (2), 139−157.

(6) Ackermann, M.; Andersen, L.; Lorenz, T.; Bohatý, L.; Becker, P. Anisotropy Study of Multiferroicity in the Pyroxene $NaFeGe_2O_6$. *New J. Phys.* **2015**, *17*, 013045.

(7) Ishii, Y.; Matsushita, Y.; Oda, M.; Yoshida, H. Structural Study of Quasi-One-Dimensional Vanadium Pyroxene $LiVSi_2O_6$ Single Crystals. *J. Solid State Chem.* **2017**, *246*, 125−129.

(8) Morimoto, N.; Fabries, J.; Ferguson, A. K.; Ginzburg, I. V.; Ross, M.; Seifert, F. A.; Zussman, J.; Aoki, K.; Gottardi, G. Nomenclature of Pyroxenes. *Mineral. Mag.* **1988**, *52*, 535−550.

(9) Nespolo, M.; Aroyo, M. I. The Modular Structure of Pyroxenes. *Eur. J. Mineral.* **2016**, *28* (1), 189−203.

(10) Cameron, M.; Papike, J. J. Structural and Chemical Variations in Pyroxenes. *Am. Mineral.* **1981**, *66*, 1−50.

(11) Thompson, R. M.; Downs, R. T. Model Pyroxenes I: Ideal Pyroxene Topologies. *Am. Mineral.* **2003**, *88* (4), 653−666.

(12) Thompson, R. M.; Downs, R. T. Model Pyroxenes II: Structural Variation as a Function of Tetrahedral Rotation. *Am. Mineral.* **2004**, *89* (4), 614−628.

(13) Arlt, T.; Kunz, M.; Stolz, J.; Armbruster, T.; Angel, R. J. P-T-X Data on $P2_1/c$-Clinopyroxenes and Their Displacive Phase Transitions. *Contrib. Mineral. Petrol.* **2000**, *138* (1), 35−45.

(14) Redhammer, G. J.; Roth, G.; Paulus, W.; André, G.; Lottermoser, W.; Amthauer, G.; Treutmann, W.; Koppelhuber-Bitschnau, B. The Crystal and Magnetic Structure of Li-Aegirine $LiFe^{3+}Si_2O_6$: A Temperature-Dependent Study. *Phys. Chem. Miner.* **2001**, *28* (5), 337−346.

(15) Redhammer, G. J.; Roth, G. Structural Variation and Crystal Chemistry of $LiMe^{3+}Si_2O_6$ Clinopyroxenes Me^{3+} = Al, Ga, Cr, V, Fe, Sc and In. *Z. Kristallogr. - Cryst. Mater.* **2004**, *219* (5), 278−294.

(16) Ullrich, A.; Schranz, W.; Miletich, R. The Nonlinear Anomalous Lattice Elasticity Associated with the High-Pressure Phase Transition in Spodumene: A High-Precision Static Compression Study. *Phys. Chem. Miner.* **2009**, *36* (10), 545−555.

(17) Periotto, B.; Angel, R. J.; Nestola, F.; Balić-Žunić, T.; Fontana, C.; Pasqual, D.; Alvaro, M.; Redhammer, G. J. High-Pressure X-Ray Study of $LiCrSi_2O_6$ Clinopyroxene and the General Compressibility Trends for Li-Clinopyroxenes. *Phys. Chem. Miner.* **2013**, *40* (5), 387−399.

(18) Mantovani, L.; Tribaudino, M.; Bertoni, G.; Salviati, G.; Bromiley, G. Solid Solutions and Phase Transitions in (Ca,M^{2+})-$M^{2+}Si_2O_6$ Pyroxenes (M^{2+} = Co, Fe, Mg). *Am. Mineral.* **2014**, *99* (4), 704−711.

(19) Yang, H.; Ghose, S. High Temperature Single Crystal X-Ray Diffraction Studies of the Ortho-Proto Phase Transition in Enstatite, $Mg_2Si_2O_6$ at 1360 K. *Phys. Chem. Miner.* **1995**, *22* (5), 300−310.

(20) Deer, W. A.; Howie, R. A.; Zussman, J. *Rock-Forming Minerals. Single-Chain Silicates*, 2nd ed.; Geological Society of London, 1997.

(21) Yang, H.; Finger, L. W.; Conrad, P. G.; Prewit, C. T.; Hazen, R. M. A New Pyroxene Structure at High Pressure: Single-Crystal X-Ray and Raman Study of the $Pbcn$-$P2_1cn$ Phase Transition in Protopyroxene. *Am. Mineral.* **1999**, *84* (3), 245−256.

(22) Redhammer, G. J.; Nestola, F.; Miletich, R. Synthetic $LiAlGe_2O_6$: The First Pyroxene with $P2_1/n$ Symmetry. *Am. Mineral.* **2012**, *97* (7), 1213−1218.

(23) Ullrich, A.; Miletich, R.; Balic-Zunic, T.; Olsen, L.; Nestola, F.; Wildner, M.; Ohashi, H. $Na,Ca)(Ti^{3+},Mg)Si_2O_6$-Clinopyroxenes at High Pressure: Influence of Cation Substitution on Elastic Behavior and Phase Transition. *Phys. Chem. Miner.* **2010**, *37* (1), 25−43.

(24) Redhammer, G. J.; Ohashi, H.; Roth, G. Single-Crystal Structure Refinement of $NaTiSi_2O_6$ Clinopyroxene at Low Temp-eratures (298 < T < 100 K). *Acta Crystallogr., Sect. B: Struct. Sci.* **2003**, *59* (6), 730−746.

(25) Angel, R. J.; Chopelas, A.; Ross, N. L. Stability of High-Density Clinoenstatite at Upper-Mantle Pressures. *Nature* **1992**, *358* (6384), 322−324.

(26) Angel, R. J.; Hugh-Jones, D. A. Equations of State and Thermodynamic Properties of Enstatite Pyroxenes. *J. Geophys. Res.* **1994**, *99* (B10), 19777−19783.

(27) Yoshiasa, A.; Nakatsuka, A.; Okube, M.; Katsura, T. Single-Crystal Metastable High-Temperature $C2/c$ Clinoenstatite Quenched Rapidly from High Temperature and High Pressure. *Acta Crystallogr., Sect. B: Struct. Sci., Cryst. Eng. Mater.* **2013**, *69* (6), 541−546.

(28) Ohashi, Y. Polysynthetically-Twinned Structures of Enstatite and Wollastonite. *Phys. Chem. Miner.* **1984**, *10* (5), 217−229.

(29) Zhang, J. S.; Dera, P.; Bass, J. D. A New High-Pressure Phase Transition in Natural Fe-Bearing Orthoenstatite. *Am. Mineral.* **2012**, *97* (7), 1070−1074.

(30) Plonka, A. M.; Dera, P.; Irmen, P.; Rivers, M. L.; Ehm, L.; Parise, J. B. β-Diopside, a New Ultrahigh-Pressure Polymorph of $CaMgSi_2O_6$ with Six-Coordinated Silicon. *Geophys. Res. Lett.* **2012**, *39* (24), 2000−2003.

(31) Pakhomova, A.; Ismailova, L.; Bykova, E.; Bykov, M.; Ballaran, T. B.; Dubrovinsky, L. A New High-Pressure Phase Transition in Clinoferrosilite: In Situ Single-Crystal X-Ray Diffraction Study. *Am. Mineral.* **2017**, *102* (3), 666−673.

(32) Lazarz, J. D.; Dera, P.; Hu, Y.; Meng, Y.; Bina, C. R.; Jacobsen, S. D. High-Pressure Phase Transitions of Clinoenstatite. *Am. Mineral.* **2019**, *104* (6), 897−904.

(33) Matsukage, K. N.; Nishihara, Y.; Karato, S. Seismological Signature of Chemical Differentiation of Earth's Upper Mantle. *J. Geophys. Res.* **2005**, *110* (B12), B12305.

(34) Akashi, A.; Nishihara, Y.; Takahashi, E.; Nakajima, Y.; Tange, Y.; Funakoshi, K. Orthoenstatite/Clinoenstatite Phase Transformation in $MgSiO_3$ at High-pressure and High-temperature Determined by in Situ X-ray Diffraction: Implications for Nature of the X Discontinuity. *J. Geophys. Res.* **2009**, *114* (B4), B04206.

(35) Arlt, T.; Angel, R. J. Displacive Phase Transitions in C-Centred Clinopyroxenes: Spodumene, $LiScSi_2O_6$ and $ZnSiO_3$. *Phys. Chem. Miner.* **2000**, *27* (10), 719−731.

(36) Sondergeld, P.; Li, B.; Schreuer, J.; Carpenter, M. A. Discontinuous Evolution of Single-Crystal Elastic Constants as a Function of Pressure through the $C2/c \leftrightarrow P2_1/c$ Phase Transition in Spodumene $(LiAlSi_2O_6)$. *J. Geophys. Res.* **2006**, *111* (B7). DOI: 10.1029/2005JB004098.

(37) Hugh-Jones, D. A.; Woodland, A. B.; Angel, R. J. The Structure of High-Pressure $C2/c$ Ferrosilite and Crystal Chemistry of High-Pressure $C2/c$ Pyroxenes. *Am. Mineral.* **1994**, *79* (11−12), 1032−1041.

(38) Nestola, F.; Redhammer, G. J.; Pamato, M. G.; Secco, L.; Dal Negro, A. High-Pressure Phase Transformation in $LiFeGe_2O_6$ Pyroxene. *Am. Mineral.* **2009**, *94* (4), 616−621.

(39) Nestola, F.; Artac, A.; Pippinger, T.; Miletich, R.; Secco, L.; Milani, S.; Redhammer, G. J. First Evidence of $P2_1/n$ to $P2_1/c$ Structural Transformation in Pyroxene-Type $LiAlGe_2O_6$ under High-Pressure Conditions. *J. Solid State Chem.* **2015**, *228*, 250−257.

(40) Hofer, G.; Kuzel, J.; Scheidl, K. S.; Redhammer, G.; Miletich, R. High-Pressure Crystallography and Compression Behavior of the Alkali-Scandium-Germanate End-Members $LiScGe_2O_6$ and $NaScGe_2O_6$. *J. Solid State Chem.* **2015**, *229*, 188−196.

(41) Miletich, R.; Allan, D. R.; Kuhs, W. F. High-Pressure Single-Crystal Techniques. *Rev. Mineral. Geochem.* **2000**, *41* (1), 445−519.

(42) Mao, H. K.; Xu, J.; Bell, P. M. Calibration of the Ruby Pressure Gauge to 800 Kbar under Quasi-Hydrostatic Conditions. *J. Geophys. Res.* **1986**, *91* (B5), 4673.

(43) Scheidl, K. S.; Miletich, R.; Kurnosov, A.; Trots, D. M.; Boffa Ballaran, T.; Angel, R. J. Extending the Single-Crystal Quartz Pressure Gauge up to Hydrostatic Pressure of 19 GPa. *J. Appl. Crystallogr.* **2016**, *49* (6), 2129−2137.

(44) King, H. E.; Finger, L. W. Diffracted Beam Crystal Centering and Its Application to High-Pressure Crystallography. *J. Appl. Crystallogr.* **1979**, *12* (4), 374−378.

(45) Angel, R. J.; Finger, L. W. SINGLE : A Program to Control Single-Crystal Diffractometers. *J. Appl. Crystallogr.* **2011**, *44* (1), 247−251.

(46) Angel, R. J. Equations of State. *Rev. Mineral. Geochem.* **2000**, *41* (1), 35−59.

(47) Angel, R. J.; Gonzalez-Platas, J.; Alvaro, M. EoSFit7c and a Fortran Module (Library) for Equation of State Calculations. *Z. Kristallogr. - Cryst. Mater.* **2014**, *229* (5), 405−419.

(48) Gonzalez-Platas, J.; Alvaro, M.; Nestola, F.; Angel, R. *EoSFit7-GUI* : A New Graphical User Interface for Equation of State Calculations, Analyses and Teaching. *J. Appl. Crystallogr.* **2016**, *49* (4), 1377−1382.

(49) Boehler, R.; De Hantsetters, K. New Anvil Designs in Diamond-Cells. *High Pressure Res.* **2004**, *24* (3), 391−396.

(50) Angel, R.; Gonzalez-Platas, J. *ABSORB-7* and *ABSORB-GUI* for Single-Crystal Absorption Corrections. *J. Appl. Crystallogr.* **2013**, *46* (1), 252−254.

(51) Sheldrick, G. M. Crystal Structure Refinement with SHELXL. *Acta Crystallogr., Sect. C: Struct. Chem.* **2015**, *71* (1), 3−8.

(52) Hübschle, C. B.; Sheldrick, G. M.; Dittrich, B. ShelXle: A Qt Graphical User Interface for SHELXL. *J. Appl. Crystallogr.* **2011**, *44* (6), 1281−1284.

(53) Gatta, D. G.; Rinaldi, R.; Knight, K. S.; Molin, G.; Artioli, G. High Temperature Structural and Thermoelastic Behaviour of Mantle Orthopyroxene: An in Situ Neutron Powder Diffraction Study. *Phys. Chem. Miner.* **2007**, *34* (3), 185−200.

(54) Schreuers, A. M. M. *MERGEHKLF5*; Utrecht University; Utrecht, The Netherlands, 2016.

(55) Spek, A. L. Structure Validation in Chemical Crystallography. *Acta Crystallogr., Sect. D: Biol. Crystallogr.* **2009**, *65* (2), 148−155.

(56) Chijioke, A. D.; Nellis, W. J.; Soldatov, A.; Silvera, I. F. The Ruby Pressure Standard to 150 GPa. *J. Appl. Phys.* **2005**, *98* (11), 114905.

(57) Huang, E.; Chen, C. H.; Huang, T.; Lin, E. H.; Xu, J. A. Raman Spectroscopic Characteristics of Mg-Fe-Ca Pyroxenes. *Am. Mineral.* **2000**, *85* (3−4), 473−479.

(58) Chopelas, A.; Serghiou, G. Spectroscopic Evidence for Pressure-Induced Phase Transitions in Diopside. *Phys. Chem. Miner.* **2002**, *29* (6), 403−408.

(59) Prencipe, M.; Mantovani, L.; Tribaudino, M.; Bersani, D.; Lottici, P. P. The Raman Spectrum of Diopside: A Comparison between Ab Initio Calculated and Experimentally Measured Frequencies. *Eur. J. Mineral.* **2012**, *24* (3), 457−464.

(60) Kroumova, E.; Aroyo, M. L.; Perez-Mato, J. M.; Kirov, A.; Capillas, C.; Ivantchev, S.; Wondratschek, H. Bilbao Crystallographic Server: Useful Databases and Tools for Phase-Transition Studies. *Phase Transitions* **2003**, *76* (1−2), 155−170.

(61) Rutstein, M. S.; White, W. B. Vibrational Spectra of High-Calcium Pyroxenes and Pyroxenoids. *Am. Mineral.* **1971**, *56*, 877−887.

(62) Pommier, C. J. S.; Denton, M. B.; Downs, R. T. Raman Spectroscopic Study of Spodumene ($LiAlSi_2O_6$) through the Pressure-Induced Phase Change From $C2/c$ to $P2_1/c$. *J. Raman Spectrosc.* **2003**, *34* (10), 769−775.

(63) Lambruschi, E.; Aliatis, I.; Mantovani, L.; Tribaudino, M.; Bersani, D.; Redhammer, G. J.; Lottici, P. P. Raman Spectroscopy of $CaM^{2+}Ge_2O_6(M^{2+}=$ Mg, Mn, Fe, Co, Ni, Zn) Clinopyroxenes. *J. Raman Spectrosc.* **2015**, *46* (6), 586−590.

(64) Ende, M.; Wunder, B.; Koch-Müller, M.; Pippinger, T.; Buth, G.; Giester, G.; Lengauer, C. L.; Libowitzky, E. T-Induced Displacive Phase Transition of End-Member Pb-Lawsonite. *Mineral. Mag.* **2016**, *80* (2), 249.

(65) Anderson, D. L.; Anderson, O. L. Brief Report: The Bulk Modulus-Volume Relationship for Oxides. *J. Geophys. Res.* **1970**, *75* (17), 3494−3500.

(66) Parsons, S. Introduction to Twinning. *Acta Crystallogr., Sect. D: Biol. Crystallogr.* **2003**, *59* (11), 1995−2003.

(67) Jahn, S. High-Pressure Phase Transitions in $MgSiO_3$ Orthoenstatite Studied by Atomistic Computer Simulation. *Am. Mineral.* **2008**, *93* (4), 528−532.